IEEJ Journal of Industry Applications
Vol.8 No.4 pp.736–744 DOI: 10.1541/ieejjia.8.736
Translated from IEEJ Transactions on Industry Applications, Vol.138 No.11 pp.848–856

Paper
(Translation of IEEJ Trans. IA)

Stability Analysis of Sensorless Speed Control for PMSM Considered Current Control System

Sari Maekawa* Member, Mariko Sugimoto* Non-member
Keiichi Ishida** Member, Masaya Nogi** Member
Masaki Kanamori** Member

For the control of permanent magnet synchronous motors, speed control, current control, sensorless control exist, and control gain design is required. In general, the control gain needs to be designed in consideration of stability and responsibility, and various researches have been conducted on this.

In this paper, the influence of the control band of the three types of control on the stability is analyzed by combining the analysis of the pole placement of the closed-loop transfer function and stability judgment considering the axial error which is the difference between the actual position and the estimated position, the relationship between each control band that can secure the results is discussed.

Keywords: PMSM, sensorless control, ASR, ACR, stability

1. Introduction

Although a method for estimating rotor magnetic flux and induced voltage in the medium to high speed range is used in sensorless control of permanent magnet synchronous motor (PMSM), various factors cause the problem of instability in sensorless control.

Instability is caused by factors due to changes in *d*-*q*-axes inductances used in rotor flux estimation occurring due to magnetic saturation [(1)–(3)] and inter-axial interference [(4)(5)], and factors due to the motor model having nonsinusoidal waveform [(6)], such as the spatial harmonics observed in motors with concentrated windings. Moreover, various studies are being conducted on topics such as the stability limit [(7)] associated with the effect of the difference between the *d*-*q*-axes inductances due to interior permanent magnet synchronous motor (IPMSM) polarity appearing as 2θ component in sensorless control, and mathematical models [(8)(19)(21)] such as the extended electromotive force model.

Furthermore, for the control gain and natural angular frequency (frequency) set in each control as required in configuring the control system based on speed command, although design methods taking into account stability have been proposed concerning methods of current control [(9)(10)], speed control [(11)(12)], and different sensorless controls [(13)–(17)], with respect to quantitative verification studies taking into account the stability of sensorless control of the control system as a whole considering the relationship between speed control and minor loop which is the frequency of current control, only studies such as on induction motor [(18)(19)] can be found, but to the best of the authors' knowledge no such study has yet been reported on permanent magnet synchronous motor.

Accordingly, with respect to the effect of frequency on the three controls of current control, speed control, and sensorless control in a permanent magnet synchronous motor sensorless control system, this study reports on determining stability using analysis of pole placement of the closed-loop transfer function, and discusses the relationship between the frequency of each control and securing stability, by considering in combination the stability judgement that takes into account the upper limit of the axial error - the difference between the actual position and the estimated position - which is a problem encountered in cases such as step load.

Section 2 describes a motor model where the simultaneous differential equation obtained form the motor voltage type and speed equation is linearized over a very short interval of time from the point of stable equilibrium, and discusses the derivation of the closed-loop transfer function and the characteristic equation of the sensorless speed control system based on the control configuration.

Section 3 explains how the poles are calculated from the estimated transfer function, and with respect to the difference in stability with that of a speed control system with sensors, compares the effect of frequency for each of the controls.

Section 4 examines the frequency of sensorless control necessary according to the theory of axial error generated in step load and its upper limit.

Section 5 verifies the validity of the proposed method, with respect to the stability constrained by the frequency of the three control systems, by comparing the results of the calculations based on the proposed method with the results of actual control tests.

* TOSHIBA CORPORATION YOKOHAMA COMPLEX
33, Shin-Isogo-cho, Isogo-ku, Yokohama, Kanagawa 235-0017, Japan
** TOSHIBA CARRIER CORPORATION FUJI FACTORY & ENGINEERING CENTER
336, Tadehara, Fuji, Shizuoka 416-8521, Japan

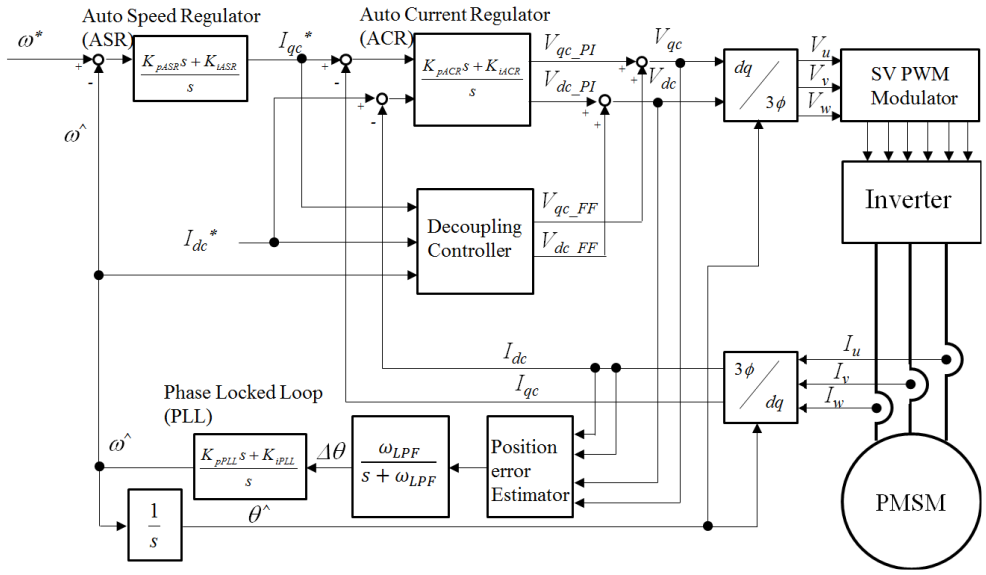

Fig. 1. Control configuration

2. Configuration of Motor and Control System

2.1 Motor Model The d-q-axes voltages of the target motor for control is given by equation (1):

$$\begin{pmatrix} V_d \\ V_q \end{pmatrix} = \begin{pmatrix} R + pL_d & -\omega L_q \\ \omega L_q & R + pL_q \end{pmatrix} \begin{pmatrix} I_d \\ I_q \end{pmatrix} + \begin{pmatrix} 0 \\ \omega\phi_f \end{pmatrix} \cdots\cdots\cdots (1)$$

where, $I_{d,q}$ are d-q-axes currents, ω is electrical frequency, $V_{d,q}$ are d-q-axes voltages, $L_{d,q}$ are d-q-axes inductances, R is winding (stator) resistance, and ϕ_f is linked flux of permanent magnet.

Moreover, the PMSM output torque T_m is given by equation (2), and the speed defined by load torque, mechanical friction, and moment of inertia can be expressed as in equation (3):

$$T_m = P\phi_f I_q + P\left(L_d - L_q\right) I_d I_q \cdots\cdots\cdots\cdots (2)$$

$$T_m - T_l = J\frac{d\omega_m}{dt} + D\omega_m \cdots\cdots\cdots\cdots\cdots (3)$$

where, ω_m is mechanical frequency, P is pole pair number, J is moment of inertia (inertia), D is friction coefficient, and T_l is load torque.

Here, by linearizing the minute changes in each state variable from a stable equilibrium point (ω_{m0}, I_{d0}, I_{q0}) in equations (1) and (3), state equation (4) can be derived.

$$\frac{d}{dt}\begin{pmatrix} \partial\omega_m \\ \partial I_d \\ \partial I_q \end{pmatrix} = \begin{pmatrix} -\dfrac{D}{J} & \dfrac{PL_1 I_{q0}}{J} & -\dfrac{P\left(\phi_f + L_1 I_{d0}\right)}{J} \\ -I_{q0} & -\dfrac{R}{L_d} & \omega\dfrac{L_q}{L_d} \\ -\dfrac{\phi_f}{L_q} & -\omega\dfrac{L_d}{L_q} & -\dfrac{R}{L_q} \end{pmatrix} \begin{pmatrix} \partial\omega_m \\ \partial I_d \\ \partial I_q \end{pmatrix} + \begin{pmatrix} 0 & 0 \\ \dfrac{1}{L_d} & 0 \\ 0 & \dfrac{1}{L_q} \end{pmatrix} \begin{pmatrix} V_d \\ V_q \end{pmatrix} = \begin{pmatrix} \dfrac{1}{J} \\ 0 \\ 0 \end{pmatrix} T_l \cdots\cdots (4)$$

where, $L_1 = L_d - L_q$.

2.2 Configuration of Control System Figure 1 shows the control configuration used in the analysis. The control method used is sensorless vector control, and utilizes speed control (auto speed regulator: ASR) based on control of motor speed command by detecting the motor current and direct current voltage. As shown in Fig. 1, sensorless control utilizes a general phase locked loop (PLL) configuration whereby, based on the voltages V_{dc}, V_{qc}, and currents I_{dc}, I_{qc} along the estimated axes d_c, q_c, axial error $\Delta\theta$ is calculated as the difference between the actual position and the estimated position, and the estimated speed $\hat{\omega}$ and position $\hat{\theta}$ are calculated using PI controllers.

Each of the controllers is a PI controller, and the auto current regulator (ACR) $C_{ACR}(s)$, the auto speed regulator (ASR) $C_{ASR}(s)$, and the PLL controller $C_{PLL}(s)$ are expressed by equations (5)~(7):

$$C_{ACR}(s) = \frac{K_{pACR}s + K_{iACR}}{s} \cdots\cdots\cdots\cdots (5)$$

$$C_{ASR}(s) = \frac{K_{pASR}s + K_{iASR}}{s} \cdots\cdots\cdots\cdots (6)$$

Moreover, the position estimation part is configured to calculate the axial error $\Delta\theta$ from the estimated information on voltage/current/speed and 1st order lag filter (low pass filter: LPF) given by equation (8):

$$C_{PLL}(s) = \frac{K_{pPLL}s + K_{iPLL}}{s} \cdots\cdots\cdots\cdots (7)$$

$$G_{LPF}(s) = \frac{\omega_{LPF}}{s + \omega_{LPF}} \cdots\cdots\cdots\cdots (8)$$

where, K_{pACR} and K_{iACR} are proportional and integral gains in current control respectively, K_{pASR} and K_{iASR} are proportional and integral gains in speed control respectively, K_{pPLL} and K_{iPLL} are proportional and integral gains in sensorless control respectively, and ω_{LPF} is the filter cut off frequency.

Here, by specifying the current controller using non-interference method along with the ones described in Refs. (9) and (10), the respective control gains can be represented by equation (9) using the frequency of ACR ω_{ACR}.

$$\begin{cases} K_{pACR} = \omega_{ACR} L_q \\ K_{iACR} = \omega_{ACR} R \end{cases} \cdots\cdots (9)$$

Moreover, since the loop transfer function in a closed loop is a second order system, using the methods described in references such as (20) and (21), gains of speed control and sensorless control are expressed by equations (10) and (11) using the respective damping coefficients ξ_{ASR} and ξ_{PLL}, and the respective frequencies of the systems ω_{ASR} and ω_{PLL}.

$$\begin{cases} K_{pASR} = 2\xi_{ASR}\omega_{ASR} J\left(\phi_f P^2\right) \\ K_{iASR} = \omega_{ASR} J\left(\phi_f P^2\right) \end{cases} \cdots\cdots (10)$$

$$\begin{cases} K_{pPLL} = 2\xi_{PLL}\omega_{PLL}^2 \\ K_{iPLL} = \omega_{PLL}^2 \end{cases} \cdots\cdots (11)$$

In the pole placement analysis to be described later, the stability is judged not using control gain but the frequencies ω_{ACR}, ω_{ASR}, and ω_{PLL} obtained using equations (9)~(11).

Next, using the controllers $C_{ACR}(s)$, $C_{ASR}(s)$, $C_{PLL}(s)$ and the motor model, the closed-loop transfer function of the sensorless control system is derived. Figure 2 shows the block diagram of the sensorless speed control. Here, for the current control system, the current control gain is defined by equation (9), and since the pole and zero point cancel each other when non-interference control operates ideally, the corresponding closed-loop transfer function $G_{ACR}(s)$ can be reduced to a lower order through simplification using equation (12):

$$G_{ACR}(s) = \frac{\omega_{ACR}}{s + \omega_{ACR}} \cdots\cdots (12)$$

Moreover, with respect to the speed control system, assuming that the friction coefficient D can be ignored being sufficiently lower compared to the moment of inertia, if the d axis current control command $I_{dc}*$ is taken as zero in a simplified configuration, the transfer function $G_1(s)$ from speed control command value $\omega*$ to actual speed ω can be expressed as in equation (13):

$$G_1(s) = C_{ASR}(s)\, G_{ACR}(s)\, P\phi_f \frac{P}{Js} \cdots\cdots (13)$$

Note that, the configuration of $I_d \neq 0$, that is, considering the case of applying d axis current control command in

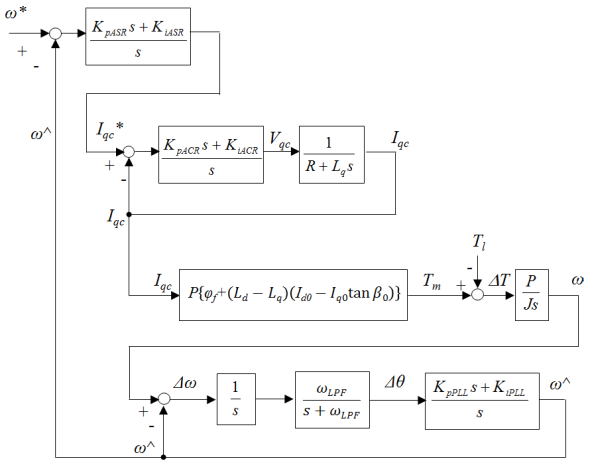

Fig. 2. Block diagram of sensorless speed control

controllers such as MTPA, if as an example a configuration is assumed where I_d* and I_q* are generated according to MTPA angle β such that I_q* = ASR output, and $I_d* = \tan(\beta) I_q*$, then the motor output torque generated from the resulting current flow, using linear approximation of the equilibrium points I_{d0} and I_{q0} in equation (4), and current phase β_0 at the point of equilibrium, is given by equation (14):

$$\Delta T_m = \Delta I_q P\left\{\phi_f + \left(L_d - L_q\right)\left(I_{d0} - \tan\beta_0 I_{q0}\right)\right\} \cdots\cdots (14)$$

Here, the transfer function $G_1(s)$ from speed command value $\omega*$ to actual speed ω is given by equation (15). Compared to equation (13), the configuration becomes complex since the reluctance torque can now be taken into account, but for a certain

$$G_1(s) = C_{ASR}(s)\, G_{ACR}(s) \times P\left\{\varphi_f + (L_d - L_q)\left(I_{d0} - I_{q0}\tan\beta_0\right)\right\} \frac{P}{Js} \cdots\cdots (15)$$

degree of saliency ratio, it is presumed that there is no problem in approximating by equation (13). For example, assuming pole pair number P = 3, ϕ_f = 0.1 Wb, L_d = 5 mH, L_q = 10 mH, equilibrium points as $I_{d0} = -3$ A and I_{q0} = 5 A, and current phase β_0 = 31 deg, although the torque coefficient for converting current into torque under the condition of $I_d = 0$ is calculated as $P\phi_f = 0.3$ in equation (13), for the aforementioned condition of $I_d \neq 0$, in equation (15) the term corresponding to saliency is incorporated causing an increase to about 0.4. In the analysis hereafter, the verification is performed using the simplified equation (13).

In addition, the closed-loop transfer function $G_{ASR^\wedge}(s)$ of estimated speed $\omega^\wedge$ corresponding to speed command value $\omega*$ including the current control, speed control, and sensorless control systems is given by equation (16).

$$G_{ASR^\wedge}(s) = \frac{\omega^\wedge}{\omega^*} = \frac{G_1(s)\, G_3(s)}{1 + G_1(s)\, G_3(s)} \cdots\cdots (16)$$

where,

$$G_2(s) = \frac{1}{s} G_{LPF}(s)\, C_{PLL}(s) \cdots\cdots (17)$$

$$G_3(s) = \frac{\omega^\wedge}{\omega} = \frac{G_2(s)}{1 + G_2(s)} \cdots\cdots (18)$$

and the characteristic equation for the closed-loop transfer function of the sensorless speed control system given by equation (16) becomes equation (19), and has six poles. Note that in case of control with sensors there are only three poles.

$$D_{AsR^\wedge}(s) = s^6 + a_5 s^5 + a_4 s^4 + a_3 s^3 + a_2 s^2 + a_1 s + a_0 \cdots\cdots (19)$$

where,

$$a_5 = \omega_{ACR} + \omega_{LPF} \cdots\cdots (20)$$

$$a_4 = \omega_{LPF}\left(2\omega_{PLL} + \omega_{ACR}\right) \cdots\cdots (21)$$

$$a_3 = \omega_{LPF}\left(\omega_{PLL}^2 + 2\xi_{PLL}\omega_{ACR}\omega_{PLL}\right) \cdots\cdots (22)$$

$$a_2 = \omega_{LPF}\omega_{ACR}\omega_{PLL}\left(\omega_{PLL} + 4\xi_{ASR}\xi_{PLL}\omega_{ASR}P^4\varphi_f^2\right) \cdots\cdots (23)$$

$$a_1 = 2\omega_{LPF}\omega_{ACR}\omega_{ASR}\omega_{PLL}P^4\varphi_f^2(\xi_{ASR}\omega_{PLL} + 4\xi_{PLL}\omega_{ASR}) \cdots\cdots (24)$$

$$a_0 = \omega_{LPF}\omega_{ACR}\omega_{ASR}^2\omega_{PLL}^2 P^4\varphi_f^2 \cdots\cdots (25)$$

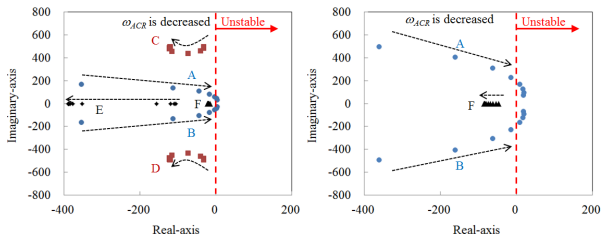

(a) Sensorless (b) With sensor

Fig. 3. Root locus when the frequency of ACR is decreased

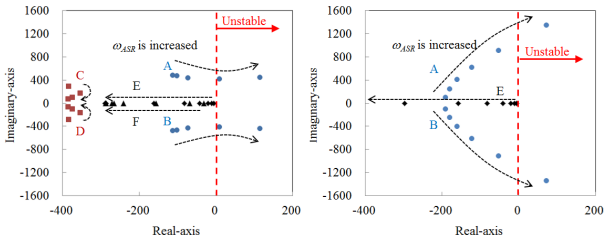

(a) Sensorless (b) With sensor

Fig. 4. Root locus when the frequency of ASR is increased

3. Stability Judgement of Sensorless Speed Control by Pole Placement

Figure 3 shows the root locus when the frequency of ACR is decreased. The graph in (a) corresponds to sensorless control, while that in (b) corresponds to control with sensors. The 4 Hz speed control frequency (frequency of ASR), the 64 Hz sensorless control frequency (frequency of PLL), and the 100 Hz cut-off frequency of low pass filter $G_{LPF}(s)$ for axial error computation are held constant, and the frequency of PLL and the LPF for axial error computation are not used in verification in (b). In all the cases, although the two poles of A and B approach the right-half of the complex plane with decrease in frequency of ACR, in sensorless control, they reach the right-half plane faster than in control with sensors. This shows that in case of sensorless control, to secure stability it is necessary to set the frequency of ACR ω_{ACR} to a value higher than what is necessary in control with sensors. Note that the three poles, pole E at a location quite distant on the negative side of real axis, and poles C and D on either side of the imaginary axis, are generated only when operating under sensorless control.

Figures 4(a) and (b) show the root locus when the frequency of ASR is increased. The 64 Hz frequency of ACR, the 64 Hz frequency of PLL, and the 100 Hz cut-off frequency of LPF $G_{LPF}(s)$ for axial error computation are held constant. Compared to current control, although the differences between sensorless control and control with sensors are small, in sensorless control, the poles A and B shift to the right-half plane resulting in instability. It is presumed that, although the poles E and F along the imaginary axis have the characteristic of moving in the opposite direction of poles A and B, since even with frequency of ACR at about 1 Hz, they do not reach the right-half plane, their effect on stability can be considered small.

Figure 5 shows the root locus when the frequency of PLL is decreased. The 64 Hz frequency of ACR, the 4 Hz frequency

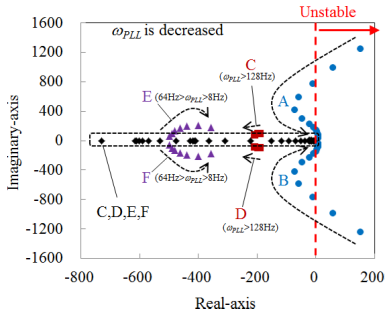

Fig. 5. Root locus when the frequency of PLL is decreased

of ASR, and the 100 Hz cut-off frequency for LPF $G_{LPF}(s)$ for axial error computation are held constant. It is revealed that the poles A and B that were tracked in Fig. 3 and Fig. 4, move along the direction of the arrows towards the right-half plane as the frequency of PLL decreases, thereby causing instability. However, even when the frequency of PLL is set excessively high, they reach the right-half plane in a similar manner, causing instability. This is due to the effect of cut-off frequency used in LPF for axial error computation, and demonstrates that the upper limit of the sensorless control frequency for stability is constrained due to LPF.

4. Limit of Frequency of Sensorless Control due to Axial Error

In the previous section the stability of the sensorless control system was analyzed using pole placement. However, in sensorless control, analysis is necessary by additionally considering the aspect of axial error limit. This becomes more prominent not in the steady state but in cases such as step load where the load torque changes rapidly causing speed change. Reference (22) proposed a control method where the axial error during acceleration is reduced using a feedback configuration. In this section, the axial error limit is analyzed using a conventional PLL method.

First, the characteristics of applying step load during sensorless control is explained by using the case shown in Fig. 6(a), where a constant current command is applied without controlling the speed. Before applying step load, the motor output torque T_m and the load torque T_l are in balance, with the difference between the two, the disturbance torque ΔT, being zero, and the speed ω is constant. When a step load is applied at time t_0, the disturbance torque ΔT generates ΔT_{max} in the negative direction, and although the actual motor speed ω and estimated speed $\hat{\omega}$ gradually decrease under a constant acceleration, there is a lag in $\hat{\omega}$ corresponding to ω due to the lag in response of the sensorless control, which results in generation of axial error $\Delta\theta$.

Here, corresponding to the block diagram of sensorless speed control in Fig. 2, the transfer function $G_4(s)$ from torque disturbance ΔT to the axial error $\Delta\theta$ can be calculated using equation (26):

$$G_4(s) = \frac{P}{Js} \frac{\dfrac{1}{s}\left(\dfrac{\omega_{LPF}}{s+\omega_{LPF}}\right)}{1+\dfrac{1}{s}\left(\dfrac{\omega_{LPF}}{s+\omega_{LPF}}\right)\left(\dfrac{K_{pPLL}s+K_{iPLL}}{s}\right)} \quad \cdots\cdots\cdots\cdots\cdots (26)$$

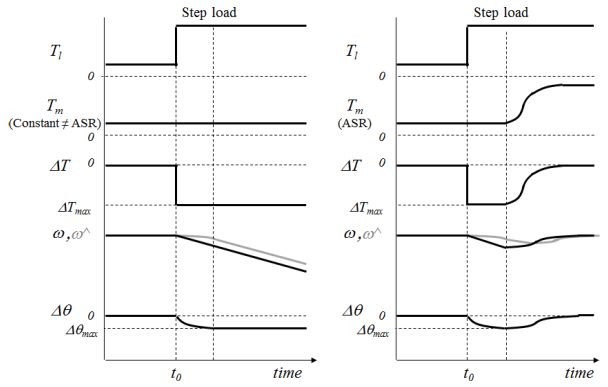

(a) Constant torque mode (b) ASR mode

Fig. 6. Transient waveform under step load

In addition, arranging the expressions of the proportional and integral gains of sensorless control using ξ_{PLL} and ω_{PLL} in equation (11), the axial error $\Delta\theta$ is given by equation (27):

$$\Delta\theta(s) = \frac{\dfrac{\Delta T P \omega_{LPF}}{J}}{s^3 + s^2\omega_{LPF} + 2\xi_{PLL}\omega_{PLL}\omega_{LPF}s + \omega_{PLL}\omega_{LPF}} \quad \cdots\cdots (27)$$

Here, corresponding to Fig. 6(a), the converged $\Delta\theta_{max}$ value for axial error $\Delta\theta$ at the time of applying step load, can be derived using the expected disturbance torque ΔT_{max}, pole pair number P, inertia J, and frequency of sensorless control ω_{PLL} in equation (28).

$$\lim_{s\to 0}\Delta\theta(s) = \frac{\Delta T_{max} P}{J\omega_{PLL}^2} \quad \cdots\cdots (28)$$

On the other hand, in case of sensorless speed control analyzed in this study, the response characteristics are as shown in Fig. 6(b). Although decrease in speed occurs corresponding to the step load, due to speed control, in an effort to hold the speed constant the motor torque increases, whereby the axial error $\Delta\theta$ converges to zero. When the the step load rise time is of the order of a few ms and is extremely fast compared to the response of the speed control, the maximum axial error generated at this time can be approximated by the sensorless loop response only similar to that in Fig. 6(a), and can be expressed as in equation (28).

Next, let us consider the allowable value of axial error $\Delta\theta$ to stabilize sensorless control under step load. When an axial error $\Delta\theta$ is generated, the actual current flow I_q along the q axis is given by equation (29) using the axial currents I_{dc} and I_{qc} along the estimated axes d_c and q_c.

Here, if $\Delta\theta$ exceeds the range $-\pi 2 \sim \pi/2$, polarity reversal occurs causing generation of negative torque in a state that needs positive torque in the speed control system, resulting in increasing the disturbance torque ΔT. That means, in equation (27), with increase in disturbance torque ΔT the axial error $\Delta\theta$ increases further. Accordingly, the allowable upper limit of $\Delta\theta$ becomes $\pi/2$. And finally, substituting $\Delta\theta < \pi/2$ in equation (28), the minimum frequency of sensorless control ω_{PLLmin} needed for stable sensorless control is given by equation (30).

Table 1. Verification conditions

Item	Value
Pole Pair number P	3
Stator resistance R	1.6 Ω
d-axis inductance L_d	12 mH
q-axis inductance L_q	15 mH
Magnetic flux ϕ_f	0.145 Wb
Inertia J	0.0003 kgm^2
Frequency of ACR f_{ACR}	16, 64, 256 Hz
Frequency of ASR f_{ASR}	1~512 Hz
Damping factor of ASR ζ_{ASR}	0.7
Frequency of PLL f_{PLL}	1~512 Hz
Damping factor of PLL ζ_{PLL}	0.7
Cut off frequency of LPF ω_{LPF}	100Hz
Control period of ACR,ASR,PLL	500 μs
Carrier frequency f_c	4kHz
Reference speed	1800 min^{-1}
Load torque T_l	0.2 Nm→1.0 Nm (ΔT_{max}=0.8 Nm)

5. Comparison of Frequency Stability Verification and Transient Response Among the Three Controls

Corresponding to the stability analysis using pole placement described in section 3, and the method of stability verification corresponding to load explained in section 4, this section discusses the confirmation of transient response operation under actual sensorless control, and the verification of validity of the proposed method.

$$\begin{pmatrix} I_d \\ I_q \end{pmatrix} = \begin{pmatrix} \cos\Delta\theta & -\sin\Delta\theta \\ \sin\Delta\theta & \cos\Delta\theta \end{pmatrix}\begin{pmatrix} I_{dc} \\ I_{qc} \end{pmatrix} \quad \cdots\cdots (29)$$

$$\omega_{PLLmin} \geq \sqrt{\frac{2\Delta T_{max} P}{\pi J}} \quad \cdots\cdots (30)$$

5.1 Verification Conditions Table 1 shows the various conditions used in the verification such as the motor, control specification, operating speed, and step load. Based on the proposed sensorless speed control stability judgement method, 6 poles can be obtained from the characteristic equation (19) used in pole analysis, and instability occurs if one of these is located on the right-half plane. Accordingly, among the 6 poles, the real part value of the one with the highest real part is confirmed, and if it is positive then it is considered unstable, but if it is negative then it is considered stable. Additionally, considering the upper limit of axial error $\Delta\theta$ from equation (30), and incorporating the stable range of frequency of sensorless control computed under verification conditions shown in Table 1, the stable range of frequencies for the three controls enabling stable sensorless speed control are also shown.

Next, the operating characteristics under step load obtained by actually operating a motor under sensorless control using the proposed method described above are compared.

Figure 7(a) shows the response waveforms of speed command value $\omega*$, estimated speed value $\omega\hat{}$, actual speed ω,

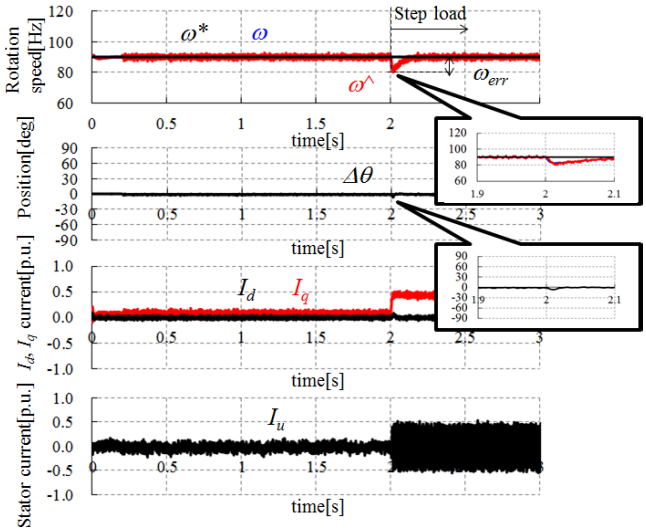

(a) The waveform when the control system is stable.
$f_{ACR} = 256\,\text{Hz}, f_{ASR} = 4\,\text{Hz}, f_{PLL} = 32\,\text{Hz}$

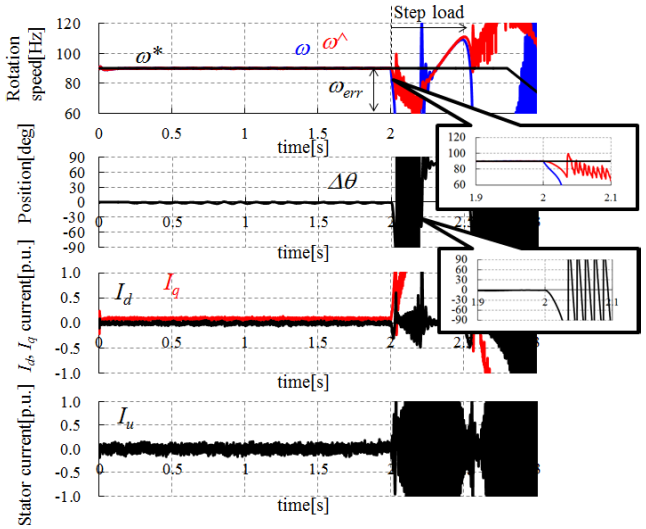

(b) The waveform when the control system is unstable.
$f_{ACR} = 256\,\text{Hz}, f_{ASR} = 4\,\text{Hz}, f_{PLL} = 4\,\text{Hz}$

Fig. 7. Transient response waveform

axial error $\Delta\theta$, the currents I_d and I_q along d and q axes, and U phase current I_u under the condition of constant speed command value and application of step load at time 2.0 s. The frequency of ACR is 256 Hz, the frequency of ACS is 4 Hz, and the frequency of PLL is 32 Hz. When the step load is applied, although the estimated speed value temporarily deviates form the speed command value, the operation of the system is stable. In contrast, Fig. 7(b) shows the results when the frequency of ACR is 256 Hz, the frequency of ASR is 4 Hz, and the frequency of PLL is 4 Hz, and with application of the step load the operation becomes unstable and the output diverges. Under such diverging conditions, since corresponding to the speed command value $\omega*$, the difference ω_{err} with the estimated speed value $\omega\hat{}$ becomes extremely large, in this study, verification was performed using the maximum value of ω_{err}, the difference between $\omega*$ and $\omega\hat{}$ used as an indicator of stability in the transient response, during the simulation period (the time span of 0~3.0 s as shown in Fig. 7). And finally, regarding the actual threshold value for

Table 2. Specification of simulator and verification conditions

Item	Verification condition	
	Test1 Fig.8(d)~(f)	Test2 Fig.8(g)~(i)
PWM harmonics	None	None
Deadtime	0μs	5μs (2% of PWM Period)
Slot harmonics	None (Sinusoidal model)	Non sinusoidal model
Magnetic saturation	None (L_q is constant.)	L_q is changed to 10% from nominal value.
Delay of voltage and current sensor	2 carrier period 500 μs	2 carrier period 500 μs
Noise of voltage and current sensor	None	Quantization noise by 12 bit AD(3LSB)
Minimum time step	1μs	1μs

judgement of stability/instability, assuming that the operation will be stopped in the event of divergence under such a speed command value, when ω_{err} exceeded $\omega*$, the system was considered to have become unstable.

5.2 Simulator Specification In verification of operation, considering the number of verifications, the results from the simulator modelling the motor and inverter were used in the study. The simulator was implemented using independently developed numerical computation.

Table 2 shows the specification of the simulator and the verification conditions. Although it is possible to incorporate the nonlinear features of the motor and the inverter in this simulator, the first set of verification is undertaken under ideal conditions. This verification confirms the efficacy of the stability range analysis taking into account the proposed method of pole analysis and upper limit of axial error. Next, in the second set of verification, the nonlinear features of the motor and inverter such as the PWM harmonics and deadtime are incorporated into the simulation, and the usefulness of the proposed method considering an actual machine is verified.

5.3 Verification Results under Ideal Conditions Figure 8(a)~(c) show the results of root locus analysis when the frequencies of ACR, ASR, and PLL are changed. When the maximum value is negative it is stable region, whereas when the maximum value is positive it is unstable region. Note that the plot scale was set such that only positive and negative are shown. As a result, it was revealed that to make the frequency of ASR high, it is necessary to increase the frequency of PLL. However, its upper limit is constrained by the frequency of ACR. Moreover, the upper limit of frequency of PLL is also constrained by the cut off frequency ω_{LPF} of the LPF of axial error. Since the cut off frequency ω_{LPF} is 100 Hz in this study, in the region with frequency of PLL higher than 100 Hz, the real part of the pole becomes positive, thereby causing instability. Moreover, the minimum frequency of PLL ω_{PLL} (f_{PLL} in the verification conditions) needed to secure stability, calculated using equation (28) with the verification conditions of this study including unexpected disturbance torque Δt_{max}, pole pair number P, and inertia J, is 11.4 Hz (71.4 rad/s), and in Figs. 8(a)~(c) the region below the dotted line shows the unstable region. That means,

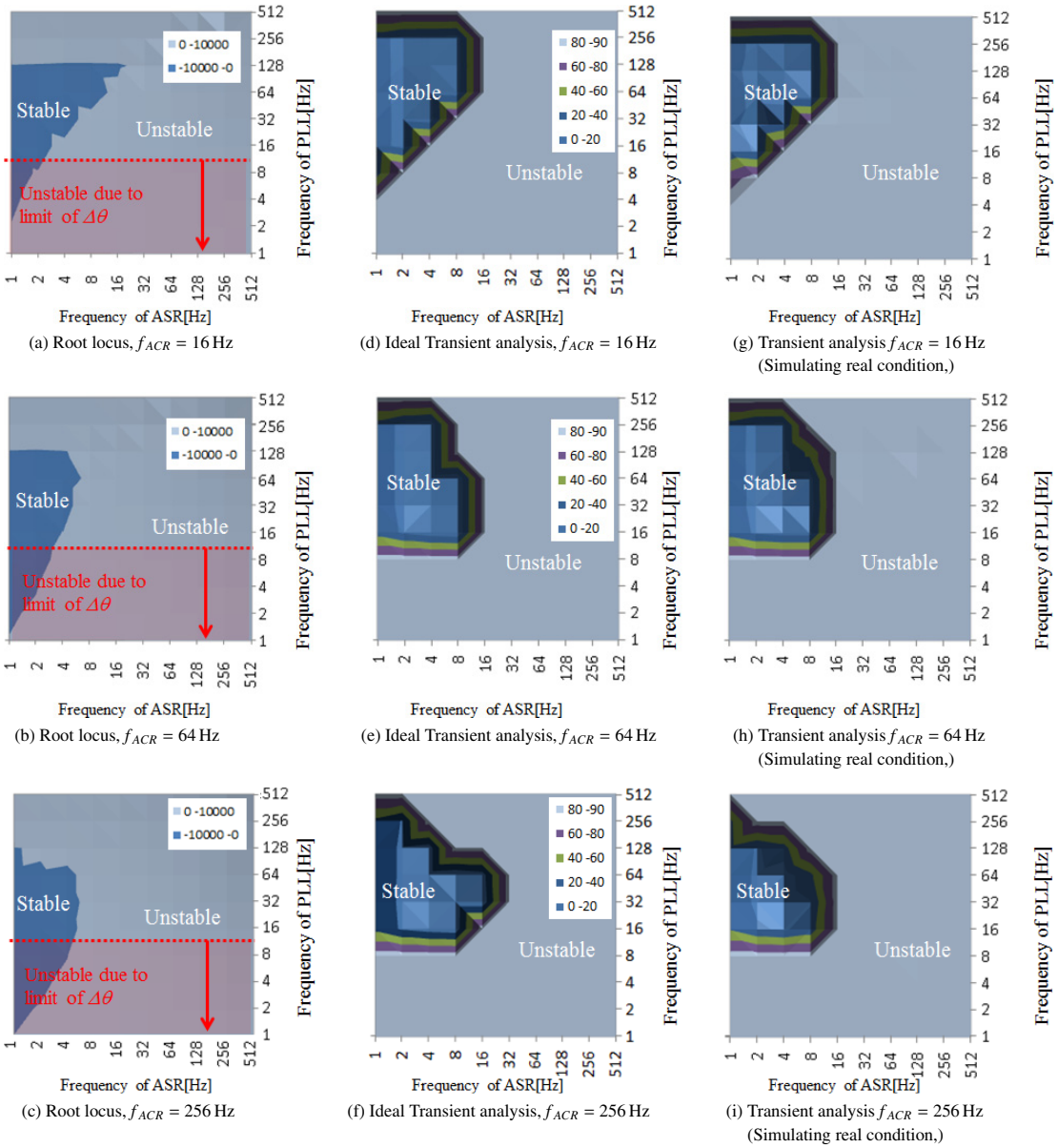

(a) Root locus, f_{ACR} = 16 Hz (d) Ideal Transient analysis, f_{ACR} = 16 Hz (g) Transient analysis f_{ACR} = 16 Hz (Simulating real condition,)

(b) Root locus, f_{ACR} = 64 Hz (e) Ideal Transient analysis, f_{ACR} = 64 Hz (h) Transient analysis f_{ACR} = 64 Hz (Simulating real condition,)

(c) Root locus, f_{ACR} = 256 Hz (f) Ideal Transient analysis, f_{ACR} = 256 Hz (i) Transient analysis f_{ACR} = 256 Hz (Simulating real condition,)

Fig. 8. The comparison of root locus analysis and transient analysis when frequencies of ACR, ASR, PLL are changed

in the analysis of placement of poles, the region of stability is constrained even furthe. Corresponding to the aforementioned results of stability analysis, plots of ω_{err} obtained in transient response tests under ideal conditions (ideal transient analysis) are shown in Figs. 8(d)~(f). The transient analysis results showed that, with increase in frequency of ACR, the trend of change in range of frequency of ASR and frequency of PLL to enable stable operation, closely agreed with the results of pole (placement) analysis. For example, as shown Fig. 8 it is observed that, in the case of frequency of PLL of 64 Hz, the frequency of ASR needed for stable operation under frequency of ACR of 64 Hz is lower than 4 Hz, and in the corresponding transient analysis results also, for a frequency lower than 8 Hz the speed change corresponding to input command is smaller, enabling stable operation without diverging. In the pole placement analysis with frequency of ACR of 256 Hz, the stable region is similarly below 4 Hz, while in the transient analysis, the stable region is below 16 Hz, which is slightly larger, but the trend is similar.

Next, the results of analysis of lower limit of frequency of PLL are compared. Substituting the verification conditions from Table 1 in equation (30), the calculated frequency of PLL for stable operation is above 11.4 Hz (71.4 rad/s), and since the transient analysis results as shown in Figs. 8(d)~(f) also indicate that the region above 16 Hz is stable, together these results confirm the usefulness of the present method.

In contrast, the upper limit of frequency PLL for stable operation constrained by the low pass filter of axial error, obtained from pole placement analysis is about two times smaller than that obtained from transient analysis. One likely reason for this is that, as shown in Fig. 5, the movements of the poles A and B near the real axis are very large, and even a slight difference in frequency of PLL can cause reaching the right-half plane making the operation unstable. In both the pole placement analysis and the transient analysis the resolution of frequency of PLL was set as multiple of 2, and it is considered likely that nearly similar results could be obtained by setting a higher resolution.

5.4 Verification Results Assuming Real Conditions

Lastly, the results of changing the motor and inverter model under ideal conditions to a more realistic model are compared be referring to Figs. 8(g)~(i). Compared to the stable range shown in Figs. 8(d)~(f), a slight decrease can be observed. Although it may be considered that the range of stable frequency has narrowed due to inclusion of nonlinear features since the proposed method assumes an ideal linear model of motor and inverter, the trends observed are nearly similar confirming that even when considering real conditions the proposed method is useful. One reason for this change in stable range is that, since significant difference is observed in case of $f_{ACR} = 256\,\mathrm{Hz}$, it may be due to the increase in disturbance in current control caused by deadtime error and motor harmonics, and the authors would like to report on this in detail in a subsequent paper.

6. Conclusion

The effect of frequency on stability in permanent magnet synchronous motor sensorless speed control system was studied for three types of control, namely, current control, speed control, and sensorless control. The characteristics of the proposed method of stability analysis are described as follows.

(1) The range of the frequency of the three controls that enable stable sensorless control can be quantitatively determined by analyzing the poles of the closed-loop transfer function from the speed command value to the estimated speed.

(2) The stable range of frequency considering transient states such as under step load, can be calculated by combining pole placement analysis with stability judgement based on upper limit of axial error.

In the aforementioned investigation, drive verification was undertaken through actual sensorless control operation, and in addition to ideal conditions, under actual conditions assuming real motors, it was confirmed that similar results could be obtained. The authors would like to study the effect of the nonlinear features on stability in the future.

References

(1) H. Kato, S. Doki, and M. Ishida: “q-axis Inductance Setting Method for SynRM’s Sensorless Control with An Extended Electromotive Force”, Industrial Application Conference of IEEJ, No.1, pp.379–382 (2005) (in Japanese)

(2) Y. Yamamoto, Y. Higashi, H. Matsuno, and S. Ogasawara: “Analysis of Unstable Regions in Vector-Controlled IPMSM Sensorless Control”, *IEEJ Trans. IA*, Vol.127-D, No.12, pp.1197–1204 (2007) (in Japanese)

(3) T. Ohnuma, S. Doki, and S. Okuma: “Inductance Setting Method for Extended EMF Observer Based on Stabilitu Analysis against Parameter Errors”, Industrial Application Conference of IEEJ, No.1, pp.569–572 (2009) (in Japanese)

(4) B. Stumberger, G. Stumberger, D. Dolinar, A. Hamler, and M. Trlep: “Evaluation of Saturation and Cross-Magnetization Effects in Interior Permanent-Magnet Synchronous Motor”, IEEE Trans. on Industry Applications, Vol.39, No.5 (2003)

(5) J. Nakatsugawa, N. Iwasaki, H. Nagura, and Y. Iwaji: “Proposal of Mathematical Models Taking into Consideration Magnetic Saturation and Cross-Coupling Effects in Permanent Magnet Synchronous Motors”, *IEEJ Trans. IA*, Vol.130, No.11, pp.1212–1220 (2010) (in Japanese)

(6) S. Jung, H. Kobayasi, S. Doki, S. Okuma, and M. Fujitsuna: “A Method for Mathematical Modeling Spatial Harmonics in a SynRM for Sensorless Control”, *IEEJ Trans. IA*, Vol.131, No.2, pp.171–179 (2011) (in Japanese)

(7) S. Ichikawa, Z. Chen, M. Tomita, S. Doki, and S. Okuma: “Sensorless Controls of Salient-Pole Permanent Magnet Synchronous Motors Using Extended Electromotive Force Models”, *IEEJ Trans. IA*, Vol.122, No.12, pp.1088–1096 (2002) (in Japanese)

(8) Y. Nakazawa, K. Kondo, S. Taniguchi, and K. Yasui: “A Position Sensorless Vector Control for Permanent-Magnet Synchronous Motor Having High Reluctance Torque Ratio”, *IEEJ Trans. IA*, Vol.135, No.6, pp.611–621 (2015) (in Japanese)

(9) K. Kondo, K. Matsuoka, and Y. Nakazawa: “A Designing Method in Current Control System of Permanent Magnet Synchronous Motor for Railway Vehicle Traction”, *IEEJ Trans. IA*, Vol.118, No.7-8, pp.900–907 (1998) (in Japanese)

(10) K. Tobari, T. Endo, Y. Iwaji, and Y. Ito: “Examination of New Vector Control System of Permanent Magnet Synchronous Motor for High-Speed Drives”, *IEEJ Trans. IA*, Vol.129, No.1, pp.36–45 (2009) (in Japanese)

(11) H. Sugimoto, M. Oyama, and S. Tamai: “Theory of AC servo system and Actual design”, pp.153–179, Sogo denshi shuppan (1990)

(12) H. Sugimoto, T. Ichikawa, K. Hosoi, and S. Kawasaki: “Magnetic Pole Position Detection Method and Control of Brushless DC Servomotor with Incremental Encoder”, *IEEJ Trans. IA*, Vol.122, No.9, pp.899–909 (2002) (in Japanese)

(13) G. Yang, R. Tomioka, M. Nakano, and T. Chin: “Position and Speed Sensorless Control of Brush-Less DC Motor Based on an Adaptive Observer”, *IEEJ Trans. IA*, Vol.113, No.5, pp.579–586 (1993) (in Japanese)

(14) T. Takeshita, M. Ichikawa, J. Lee, and N. Matsui: “Back EMF Estimation-Based Sensorless Salient-Pole Brushless DC Motor Drives”, *IEEJ Trans. IA*, Vol.117, No.1, pp.98–104 (1997) (in Japanese)

(15) S. Shinnaka: “New Sensorless Vector Control Methods Based on a New Minimum-Order Flux State-Observer in the “D-Module” for Permanent Magnet Synchronous Motors”, *IEEJ Trans. IA*, Vol.123, No.12, pp.1446–1460 (2003) (in Japanese)

(16) Y. Yamamoto, Y. Yoshida, and T. Ashikaga: “Sensor-less Control of PM Motor using Full Order Flux Observer”, *IEEJ Trans. IA*, Vol.124, No.8, pp.743–749 (2004) (in Japanese)

(17) M. Hasegawa, H. Yamauchi, and K. Matsui: “Improvement in Response of IPMSM Position Sensorless Control Using Adaptive Observer Based on Direct-Type Adaptive Control”, *IEEJ Trans. IA*, Vol.131, No.1, pp.9–16 (2011) (in Japanese)

(18) K. Ohyama, K. Shinohara, T. Nagano, and H. Arima: “Stability Analysis of the Direct Field Oriented Control System of the Induction Motor without a Speed Sensor using the Adaptive Rotor Flux Observer”, *IEEJ Trans. IA*, Vol.119, No.3, pp.333–344 (1999) (in Japanese)

(19) K. Shinohara, T. Nagano, and K. Ohyama: “Stability Analysis of Vector Control of Induction Motor without Speed Sensor Taking into Account the Effects of Current Control Loop”, *IEEJ Trans. IA*, Vol.116, No.3, pp.337–347 (1996) (in Japanese)

(20) S. Morimoto, K. Kawamoto, and Y. Takeda: “Position and Speed Sensorless Control for IPMSM Based on Estimation of Position Error”, *IEEJ Trans. IA*, Vol.122, No.7, pp.722–729 (2002) (in Japanese)

(21) K. Tanaka and I. Miki: “Position Sensorless Control of Interior Permanent Magnet Synchronous Motor Using Extended Electromotive Force”, *IEEJ Trans. IA*, Vol.125, No.9, pp.833–838 (2005) (in Japanese)

(22) K. Tobari, T. Endo, and K. Sakamoto: “A Position Error Reduction Technique for Position Sensorless Permanent Magnet Synchronous Motor Drive Systems”, Industrial Application Conference of IEEJ, No.1, pp.379–382 (2005) (in Japanese)

Sari Maekawa (Member) received a Master’s degree in electrical engineering from Hosei University. In April of the same year, he went to work for Toshiba. In April 2014, he received a Doctorate Degree from the Graduate School of Science and Technology at Meiji University. In 2019, he joined the Faculty of Science and Technology of Seikei University, as an associate professor. He is primarily engaged in the research and development of power electronics, EMI, and motor drives. In 2013, Dr. Maekawa received an IEEJ Best Paper Award (Award A) and an IEEJ Industry Applications Society Best Presentation Award. He also received the Ichimura Industry Award from the New Technology Development Foundation in 2014. His Doctorate degree is in engineering. Dr. Maekawa is a member of IEEE.

Mariko Sugimoto (Non-member) received the B.E., M.E. degrees in electrical engineering from Tokyo Institute of Technology, Japan, in 2004, and 2006, respectively. She is with Toshiba Corporation, Japan, and has been working on the development of permanent magnet synchronous motor and magnetic application products.

Keiichi Ishida (Member) received the B.E., M.E. degrees in electrical engineering from Nagaoka University of Technology, Japan, in 2002, and 2004, respectively. He is with Toshiba Carrier Corporation, Japan, and has been working on the development of the inverter for air conditioners. Mr. Ishida received the Institute of Electrical Engineers of Japan (IEEJ) Excellent Presentation Award in 2007. He also received the Electrical Science and Engineering Promotion Awards in 2016.

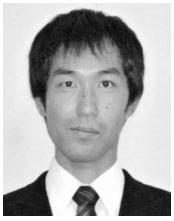

Masaya Nogi (Member) received the associate degree in electrical engineering from National Institute of Technology, Numazu College, Japan, in 2002. He is with Toshiba Carrier Corporation, Japan, and has been working on the development of the inverter for air conditioner.

Masaki Kanamori (Member) received the B.E., M.E. degrees in electrical engineering from Shizuoka University, Japan, in 2007, and 2009, respectively. He is with Toshiba Carrier Corporation, Japan, and has been working on the development of the inverter for air conditioner.